Check for updates

High-throughput CO-to-acetate electroconversion using current-dependent reconstructed Cu grain boundaries†

Peng Qiu,‡[a] Mengjiao Li,‡[b] Wenxuan Li,[a] Ziyun Wang (iD) *[b] and Yuanjie Pang (iD) *[a]

Electrochemical CO reduction (COR) offers a sustainable route for the highly selective production of high-value multi-carbon products at low current densities. However, achieving industrial-scale production remains challenging, as reconciling high current densities (>1 A cm^{-2}) with product selectivity has yet to be realized. The realization of COR at ampere-level currents for acetic acid production remains hindered by the insufficient availability of highly active sites needed to facilitate CO coupling under high-flux conditions. Here, we developed a copper oxybromide catalyst that *in situ* generates a high density of grain boundaries (GBs) during COR, as evidenced by high-resolution TEM. Density functional theory calculations verified the high activities of GB-rich surfaces due to stronger *CO adsorption compared to flat Cu(111). Coupled with pressurized CO (10 atm), these rich GBs can effectively adsorb CO and promote this coupling, further leading to a record acetic acid partial current density of 2 A cm^{-2} (67% faradaic efficiency at 3 A cm^{-2} total current), outperforming the state-of-the-art Cu-based catalysts. This work introduces an effective catalyst for enabling industrial-scale COR, highlighting the critical role of structural design in achieving high-performance electrochemical conversion.

1. Introduction

The electrochemical conversion of carbon dioxide (CO_2) has emerged as a pivotal strategy for achieving renewable energy storage and carbon neutrality goals.[1–5] This approach gains particular significance when targeting multi-carbon compounds like acetic acid, which holds dual advantages of high energy density (8.8 MJ kg^{-1}) and substantial industrial demand.[6] As a cornerstone chemical, acetate production reached 21.75 million tons globally in 2021, with projections indicating growth to 24.5 million tons by 2025. However, conventional production methods currently require energy inputs equivalent to 190 million barrels of crude oil while emitting 80 million tons of CO_2 annually.[7–9] This striking energy-environment paradox highlights the critical need for developing electrochemical CO_2-to-acetate pathways as a sustainable alternative to traditional fossil-dependent processes.

[a] School of Optical and Electronic Information, Wuhan National Laboratory for Optoelectronics, Huazhong University of Science and Technology, Wuhan 430074, China. E-mail: qiup@hust.edu.cn, d202180861@hust.edu.cn, yuanjie_pang@hust.edu.cn
[b] School of Chemical Sciences, The University of Auckland, Auckland 1010, New Zealand. E-mail: mli368@aucklanduni.ac.nz, ziyun.wang@auckland.ac.nz
† Electronic supplementary information (ESI) available. See DOI: https://doi.org/10.1039/d5lf00128e
‡ Contributed equally to this work.

The emerging tandem CO_2 reduction (CO_2R) architecture, which decouples CO_2-to-CO and CO-to-C$_{2+}$ steps from CO_2R, presents a strategic solution to chronic carbonate formation challenges in conventional single-cell systems.[10–13] A critical breakthrough lies in the first-step conversion of CO_2 to CO, achieving an exceptional faradaic efficiency exceeding 90% at current densities exceeding 800 mA cm^{-2} using solid oxide electrolysis cells.[14] This performance benchmark creates new imperatives for system integration, as commercial viability fundamentally depends on sustaining equivalent current densities throughout downstream C$_{2+}$ synthesis. Elevated current densities mean increasing acetate production rates while preserving energy efficiency metrics.[15] However, industrial viability demands matching the high current density of upstream CO generation with downstream C$_{2+}$ synthesis, a challenge unmet by conventional catalysts.

Despite advancements in pressurized COR systems that ensure sufficient CO mass transport (*e.g.*, 10 atm CO partial pressure), achieving industrial-grade current densities remains constrained by inadequate *CO adsorption and activation capacity of conventional catalysts. For copper-based systems, conventional active site architectures fail to dynamically adapt to the *CO flux demand under high currents, including engineering Cu facets,[16] alloying,[17,18] molecular tuning, *etc.*[19] The corresponding faradaic efficiency will reduce when operating at more negative

© 2025 The Author(s). Published by the Royal Society of Chemistry

RSC Appl. Interfaces, 2025, **2**, 1417–1423 | **1417**

potentials with commercially viable current densities (>1 A cm^{-2}).

Recent breakthroughs demonstrate that grain boundaries (GBs) can overcome these limitations.[20–23] Grain boundaries can be introduced through reduction reactions,[24–26] pulsing,[27] melting methods,[28] and even doping.[29] Since grain boundaries can provide undercoordinated reaction microenvironments, which favor *CO adsorption and C–C coupling, they have received widespread attention.[30] For instance, Cu nanoparticles with engineered GBs achieved 87% C$_{2+}$ faradaic efficiency at 768 mA cm^{-2} in membrane electrode assemblies, where *operando* Raman spectroscopy confirmed that GBs stabilize *OCCOH intermediates and suppress the HER.[28] However, the relationship between the grain boundary density and reaction rate is often neglected. This oversight is particularly critical because optimal catalytic performance likely requires dynamic matching between the population of active sites (governed by the GB density) and electron flux (determined by the current density). An insufficient GB density at high current densities may lead to the HER.[31] The absence of such fundamental understanding hinders the rational design of GB-engineered catalysts for practical applications across varying operational scales.

Herein, we propose a catalyst that applied current density that serves as a dynamic stimulus, driving surface restructuring and grain fragmentation in a density-dependent manner. By employing a low-crystallinity copper oxybromide precursor, the GB density is intrinsically coupled to the applied current, ensuring that active site generation aligns with the reaction rate. Pressurized operation (10 atm) further enhances CO availability while stabilizing GB configurations against interfacial degradation. This synergy enables the copper oxybromide catalyst to exhibit a high acetate selectivity over a wide range of current densities. The electrocatalyst enables a remarkable faradaic efficiency of 67% for CO-to-acetate electroreduction and an ultra-high acetate partial current density of 2 A cm^{-2}.

2. Experimental section

2.1. Materials

The precursor chemicals used in this work were *N,N*-dimethylformamide (DMF), cupric bromide (CuBr$_2$, $>99.9\%$), propanone, propylene oxide, sodium hydroxide (NaOH, 99%), and copper oxide (CuO, 99%). All the chemicals were used without further purification.

2.2. Synthesis of Cu$_2$(OH)$_3$Br

Cu$_2$(OH)$_3$Br catalysts were synthesized through a sol–gel method. CuBr$_2$ (0.5 mmol) was first dissolved in DMF (7.5 mL) in a vial and stirred thoroughly. Deionized water (0.2 mL) and propylene oxide (4.2 mL) were added simultaneously into the dissolved cupric bromide solution under stirring. The solution color changed gradually from brown to dark green. After allowing it to stand for 12 h,

the gel was washed multiple times with acetone solution. Finally, the catalyst was placed in a vacuum oven for 12 h at 60 °C to dry. The reaction mechanism is shown below.[32]
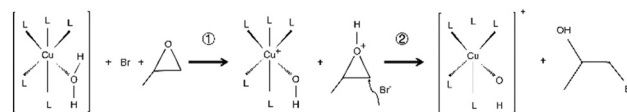
2.3. Quantification of the GB density from TEM images

GB densities of GBs-Cu-300, GBs-Cu-700, GBs-Cu-1000 and annealed GBs-Cu catalysts were measured using the method described below. GBs are considered as the border of two regions with different lattice orientations and are marked with yellow lines in the TEM images. For each sample, ten typical TEM images are analyzed. The fragmented area (S_i) is defined as the surface area of the same crystal boundary orientation enclosed by the yellow circle. The grain boundary length (L) is defined as the total length of the yellow line segments. The fragmented area and the length of the grain boundaries were both calculated using AutoCAD. Assuming that the surface GB density is calculated using the following equation:

$$\frac{\text{Grain boundary length}}{\text{Surface area}} = \frac{\sum L}{\sum S_i}$$

2.4. Density functional theory calculations

All calculations are based on density functional theory (DFT) within the exchange and correlation potentials of Perdew–Burke–Ernzerhof (PBE) as implemented in the Vienna *ab initio* simulation package (VASP).[33–35] The projector augmented wave (PAW) method with a plane-wave basis set was employed to describe the force between ion cores and valence electrons. The dispersion corrections in Grimme's scheme (DFT-D3) were employed to treat the long-range interactions between slabs and adsorbates.[36–38] The Cu(111) and Cu(111)-twin were constructed using p(3×3) metal slabs. A 10 Å vacuum slab along the *z*-axis was established between the two slabs to avoid the virtual periodic interactions. All structures are optimized to fix the bottom two layers, allowing the top two layers to fully relax. The cut-off energy of the plane-wave basis was set to 400 eV in our DFT calculations. A Γ-centered Monkhorst–Pack $3 \times 3 \times 1$ k-point grid was utilized to sample in the Brillouin zone during optimization. The convergent can be achieved with the energy and force convergence criteria set at 10^{-5} eV and 0.05 eV Å^{-1}, respectively.

The free energy change for different intermediates involved in the COR process is calculated using the following equation:

$$\Delta G = \Delta E + \Delta E_{ZPE} - T\Delta S$$

where ΔE represents the energy from DFT calculations, and ΔE_{ZPE} and ΔS indicate the zero-point energy and the change of entropy, respectively.

The adsorption energy (ΔE_{ads}) of CO can be calculated according to the following equation:

$$\Delta E_{ads} = E_{total} + E_{slab} - E_{CO}$$

where E_{total} is the total energy of the adsorbate adsorbed on slabs, E_{slab} is the energy of Cu(111) or the Cu(111)-twin and E_{CO} is the energy of the free adsorbate before adsorption.

3. Results and discussion

3.1. Catalyst synthesis and physical characterization

The initial $Cu_2(OH)_3Br$ catalyst was synthesized *via* an epoxide-assisted hydrolysis method, with the phase purity confirmed by X-ray diffraction (XRD) analysis (PDF#45-1309, Fig. 1a and S1†).[39] The scanning electron microscopy (SEM) image reveals a hierarchical architecture composed of interlinked nano-plates (Fig. 1b), while the XPS pattern confirmed the uniform surface distribution of Cu, O, and Br atoms (Fig. 1c and S2†). The pre-catalyst was uniformly deposited onto a gas diffusion electrode (GDE) *via* spray coating, followed by electrochemical reduction at −0.64 V *versus* RHE for 2 minutes. This treatment successfully converted the precursor into metallic copper, as confirmed by the distinct Cu(111), Cu(100), and Cu(110) peaks (Fig. 1d). Time-resolved SEM captured the dynamic morphological evolution during reduction, driven by Br⁻ leaching – a mechanism corroborated by the structural stability of $Cu(OH)_2$ and CuO controls under identical conditions (Fig. 1e, f and S3†).[40]

3.2. Grain boundary statistics and DFT calculations

The as-synthesized catalysts were subjected to electrochemical reduction at current densities of 300, 700 and 1000 mA cm⁻² for 5 minutes, yielding the final catalysts denoted as GBs-Cu-*x* (where *x* represents the applied current density). Energy-dispersive X-ray spectroscopy (EDS) confirmed the absence of residual Br⁻ species in all samples (Fig. S4†), verifying the thoroughness of the restructuring process. At a current density of 300 mA cm⁻², large nanoparticles aggregated to form dendritic structures. As the current density increased, the accelerated Br⁻ leaching rate shortened the reconstruction time of surface Cu ions, thereby reducing the surface particle size. Upon reaching 1000 mA cm⁻², the ultra-fine particles embedded within nanosheet-derived porous networks, as visualized in Fig. 2a–c. High-resolution transmission electron microscopy (HRTEM) provided deeper insights into the *in situ* reconstruction. The grain boundary area quantified 65 nm² at 300 mA cm⁻², and then progressively diminished from 45 to 33 nm² as the current intensified from 700 to 1000 mA cm⁻². The grain boundary density exhibited an inverse correlation, increasing from 331 to 414 μm⁻¹, demonstrating current-modulated catalyst restructuring (Fig. 2d–h and S5–S7†).

The OH⁻ adsorption spectral measurements conducted in 1.0 M KOH indicated the Cu(100), Cu(110) and Cu(111) facets, respectively, and have very similar intensities for the GBs-Cu-*x* (*x* = 300, 700 and 1000) catalysts (Fig. 3a and S8†). However, the electrochemical active surface areas (ECSAs) of GBs-Cu-*x* enlarge with an increasing current density, and this conclusion was consistent with the crystal boundary density we obtained from TEM statistics (Fig. 3b and S9†). To provide in-depth insights into the role of GBs in C–C coupling, *operando* Raman spectroscopy was used to study the surface-
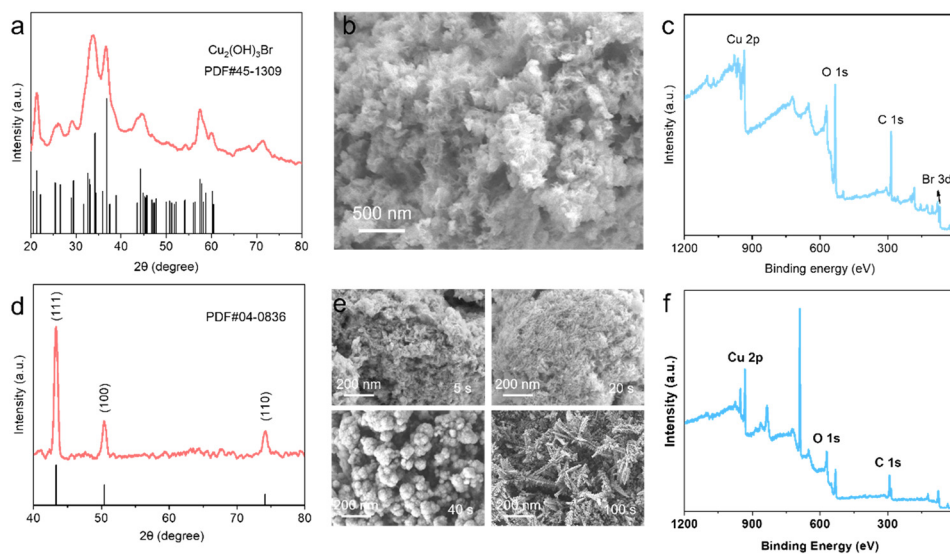

Fig. 1 Preparation and characterization of the $Cu_2(OH)_3Br$ and pure Cu catalysts. (a) XRD pattern, (b) SEM image and (c) XPS pattern of $Cu_2(OH)_3Br$. (d) XRD pattern, (e) SEM images and the (f) XPS pattern of the pure Cu catalyst.
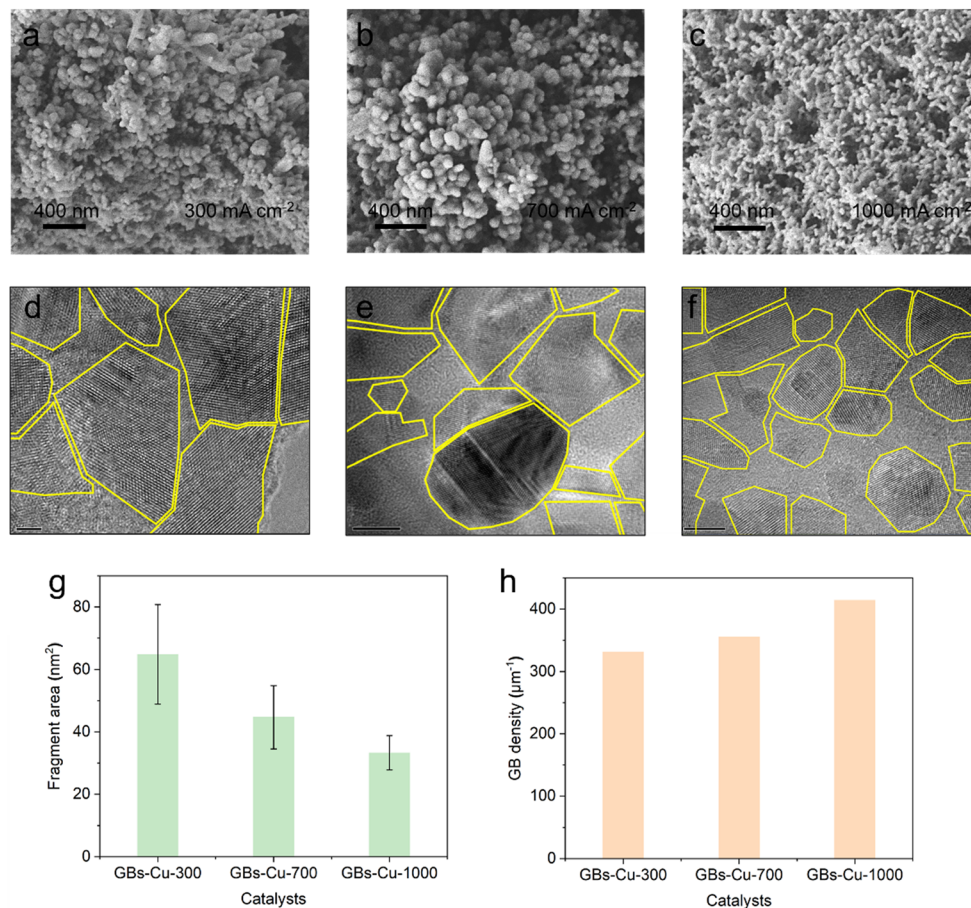
Fig. 2 SEM images of (a) GBs-Cu-300, (b) GBs-Cu-700 and (c) GBs-Cu-1000. HRTEM images of (d) GBs-Cu-300, (e) GBs-Cu-700 and (f) GBs-Cu-1000. (g) Fragment areas and (h) GB densities of GBs-Cu-*x* (*x* represents 300, 700 and 1000).
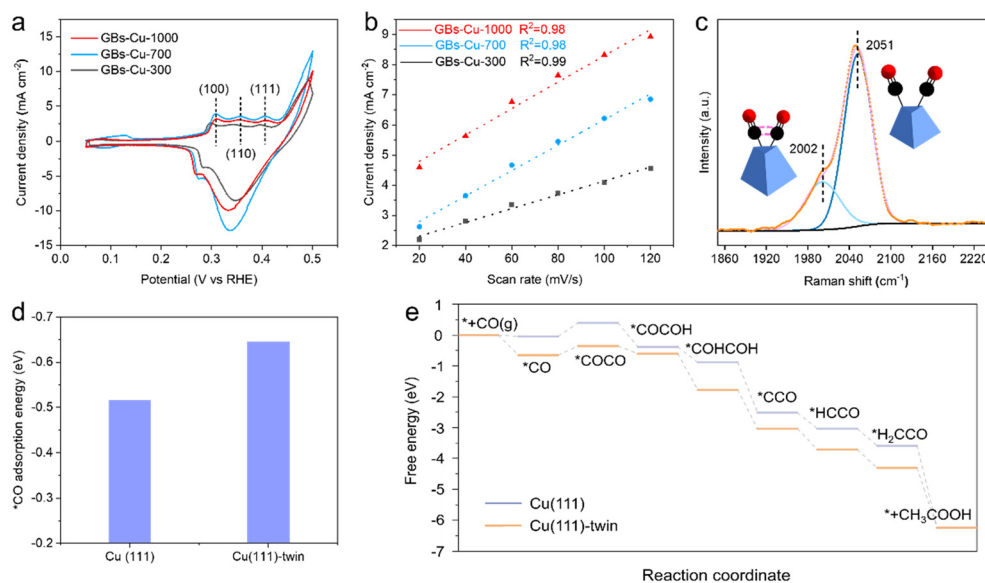

Fig. 3 (a) OH⁻ adsorption spectral measurements and (b) double layer capacitance comparison of GBs-Cu-*x* (*x* represents 300, 700 and 1000). (c) *In situ* Raman spectroscopy of GBs-Cu-300 under CO electrolysis at −1.3 V *versus* Ag/AgCl. (d) *CO adsorption energy on Cu(111) and the Cu(111)-twin. (e) The energy profiles towards acetate formation on Cu(111) and the Cu(111)-twin.

1420 | *RSC Appl. Interfaces*, 2025, **2**, 1417–1423

© 2025 The Author(s). Published by the Royal Society of Chemistry

adsorbed intermediates during CO electrolysis. Compared to the reduced $Cu(OH)_2$ catalyst, GBs-Cu-300 showed a red shift in the dominant *CO band and a stronger surface-enhanced Raman scattering signal, indicating stronger *CO binding (Fig. S10†). At −1.3 V vs. Ag/AgCl, GBs-Cu-300 exhibited distinct vibrational bands: a low-frequency (LF) *CO peak at 2002 cm^{-1} (step-edge adsorption) and a high-frequency (HF) *CO peak at 2051 cm^{-1} (isolated adsorption). A prior study shows that this dynamic LF-CO is the active *CO intermediate for C_{2+} product formation (Fig. 3c).[41] Furthermore, we investigated the role of the GBs in promoting C–C coupling and tuning the selectivity among C_{2+} products using DFT calculations. We built three GB models for the Cu(111)-twin, Cu(100)-twin, and Cu(111)/(100)-twin, respectively (Fig. S11†). Taking the Cu(111)-twin as an example, it can be seen that *CO adsorption at the Cu(111)-twin is significantly stronger ($\Delta G_{*CO} = −0.64$ eV) than at the single Cu(111) facet ($\Delta G_{*CO} = −0.51$ eV) (Fig. 3d). The energy profiles towards acetate formation on the Cu(111)-twin and Cu(111) are shown in Fig. 3e. We further investigated the *CO adsorption and energy profiles on the Cu(100)-twin and Cu(111)/(100)-twin, which indicates that the CO adsorption capacity is significantly improved on GBs (Fig. S12–S15†). These results prove that grain boundaries play a key role in *CO adsorption and C–C coupling.

3.3. Electrochemical CORR and acetate selectivity

We systematically investigated COR performance in a flow cell with systematic pressure operation. Under ambient pressure conditions with a 5.0 M KOH electrolyte, the catalyst achieved an 80% FE for C_{2+} products, yet acetate selectivity remained limited to 16.3%, indicating an unsuitable acetate production microenvironment. Remarkably, increasing the pressure to 10 atm boosted the acetate FE to 80%, a nearly fivefold enhancement attributed to increased *CO surface coverage. However, further pressurization beyond 10 atm yielded no additional selectivity improvements, confirming that *CO coverage saturation had been achieved (Fig. 4a and S16†). Besides, the morphology and the crystal structure are well preserved, as well as the maintenance of abundant GBs, as shown in HR-TEM images, suggesting that the catalyst has good stability during the CORR process (Fig. S17–S19†). Building on these pressure-dependent insights, we systematically investigated the current density effects across a wide operational range (200–3500 mA cm^{-2}). The grain boundary density, governed by the current density, ensures dynamic matching between the number of active sites and reaction rates across varying current densities, resulting in exceptional acetate performance throughout extreme current density ranges. As shown in Fig. 4b, the catalyst maintained exceptional acetate selectivity, achieving a record partial
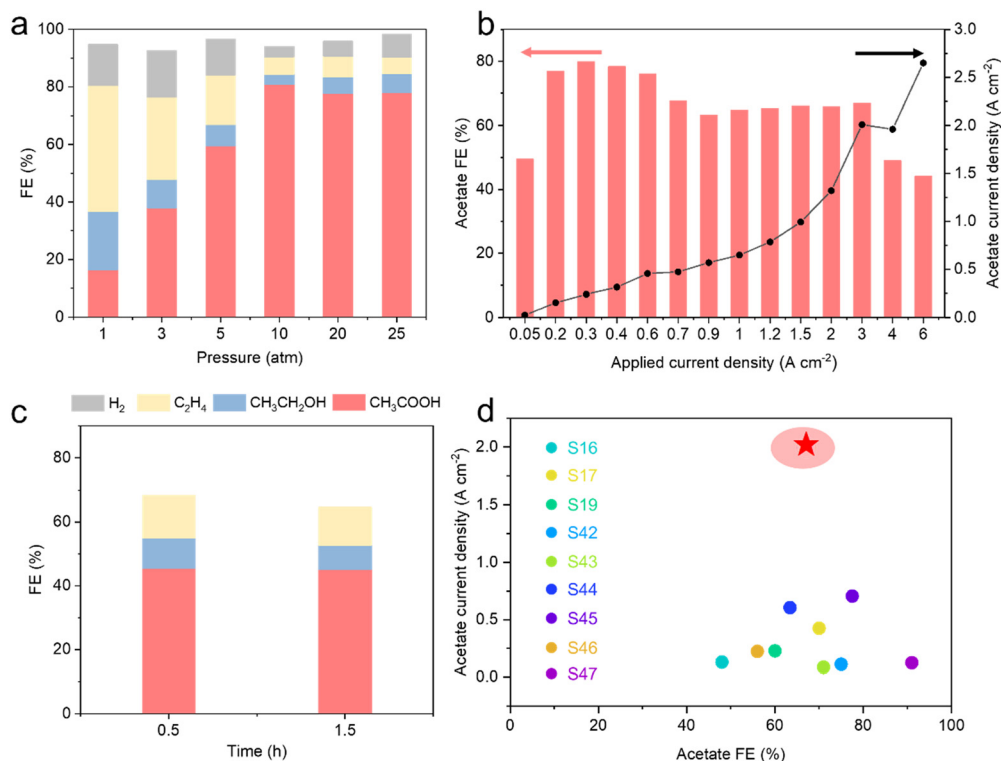

Fig. 4 CORR performance of different cathode electrodes in a flow cell. (a) FEs for various products of $Cu_2(OH)_3Br$ at −0.64 V versus RHE under different pressures. (b) FEs for various products as a function of total current over $Cu_2(OH)_3Br$. (c) FEs for various products of annealed GBs-Cu (annealing temperature = 300 °C). (d) Comparison of the catalytic performance of $Cu_2(OH)_3Br$ with those recently reported outstanding Cu-based catalysts.[16,17,19,42–47]

current density of 2000 mA cm^{-2} – a performance benchmark surpassing prior reports. As a control, GBs-Cu-300 annealed at 300 °C showed a significantly reduced grain boundary density, resulting in a sharp decrease in the acetic acid faradaic efficiency ($\leq$ 45% acetic acid FE with a 5.0 M KOH electrolyte at 10 atm). This contrast directly confirms the indispensable role of grain boundaries in sustaining high-current operation (Fig. 4c and S20, Table S1†). As shown in Fig. 4d, compared with the reported state-of-the-art electrocatalysts evaluated in a flow cell, the Cu$_2$(OH)$_3$Br exhibits outstanding electroconversion performance, especially operated at a high current density (over 1000 mA cm^{-2}), indicating the high-rate production of acetate.

4. Conclusions

In summary, this work demonstrates that sufficient active site density is critical for achieving high selectivity under industrially relevant current densities. Contrary to previous studies that focused on inhibiting catalyst reconstruction, we strategically leveraged the reduction current as a dynamic driver to activate *in situ* surface reconstruction precisely during the reaction initiation phase, thereby generating precisely tailored active sites. Through TEM images coupled with electrochemical active surface area measurements, we discovered that the *in situ* generated grain boundary density dynamically adapts to the applied current density, achieving real-time matching with the reaction rate. By synergistically combining grain boundary engineering with pressurization, the catalyst achieved unprecedented acetic acid selectivity across a broad current range (200–3500 mA cm^{-2}), including a record 2 A cm^{-2} partial current density. This study establishes an innovative design paradigm for highly selective and efficient copper-based catalysts, advancing the frontier of electrochemical acetate production.

Data availability

All data supporting this study are available within the article and its ESI.† Additional raw/processed data required to reproduce these findings can be obtained from the corresponding author upon reasonable request.

Author contributions

Peng Qiu: investigation and writing – original draft; Mengjiao Li: methodology and investigation; Wenxuan Li: investigation, formal analysis, and data curation; Ziyun Wang: resources, writing – review & editing, and supervision; Yuanjie Pang: conceptualization, supervision, methodology, resources, visualization, funding acquisition, project administration, and writing – review & editing.

Conflicts of interest

The authors declare that they have no known competing financial interests or personal relationships that could have appeared to influence the work reported in this paper.

Acknowledgements

Notes and references

1 D. Wakerley, S. Lamaison, J. Wicks, A. Clemens, J. Feaster, D. Corral, S. A. Jaffer, A. Sarkar, M. Fontecave, E. B. Duoss, S. Baker, E. H. Sargent, T. F. Jaramillo and C. Hahn, *Nat. Energy*, 2022, **7**, 130–143.

2 S. Hu, Y. Chen, Z. Zhang, S. Li, H. Liu, X. Kang, J. Liu, S. Ge, J. Wang, W. Lv, Z. Zeng, X. Zou, Q. Yu and B. Liu, *Small*, 2024, **20**, e2308226.

3 T. Yang, Y. Zhang, J. Shi, G. Yang, J. Dang, M. Sun, A. Arshad, N. Zafar and S. Yun, *J. Mater. Chem. A*, 2025, **13**, 5400.

4 P. Luna, C. Hahn, D. Higgins, S. A. Jaffer, T. F. Jaramillo and E. H. Sargent, *Science*, 2019, **364**, 350.

5 L. Bian, Y. Bai, J. Chen, H. Guo, S. Liu, H. Tian, N. Tian and Z. Wang, *ACS Nano*, 2025, **19**, 9304–9316.

6 L. Lv, Y. Shen, M. Zhou, Y. Zhang, X. Meng, X. Yang, N. Zhang, K. Wang, Q. He, D. Gong, Q. Ai, Y. Shuai and Z. Zhou, *J. Mater. Chem. A*, 2024, **12**, 6733.

7 H. Shin, K. U. Hansen and F. Jiao, *Nat. Sustain.*, 2021, **4**, 911–919.

8 D. Gao, R. M. Arán-Ais, H. S. Jeon and B. Roldan Cuenya, *Nat. Catal.*, 2019, **2**, 198–210.

9 X. Zhi, Y. Jiao, Y. Zheng, A. Vasileff and S. Qiao, *Nano Energy*, 2020, **71**, 104601.

10 W. Ma, X. He, W. Wang, S. Xie, Q. Zhang and Y. Wang, *Chem. Soc. Rev.*, 2021, **50**, 12897–12914.

11 M. Jouny, W. Luc and F. Jiao, *Nat. Catal.*, 2018, **1**, 748–755.

12 M. Jouny, G. S. Hutchings and F. Jiao, *Nat. Catal.*, 2019, **2**, 1062–1070.

13 S. Jin, Z. Hao, K. Zhang, Z. Yan and J. Chen, *Angew. Chem., Int. Ed.*, 2021, **60**, 20627–20648.

14 A. Hauch, R. Küngas, P. Blennow, A. B. Hansen, J. B. Hansen, B. V. Mathiesen and M. B. Mogensen, *Science*, 2020, **370**, 186.

15 X. Yu, Y. Xu, L. Li, M. Zhang, W. Qin, F. Che and M. Zhong, *Nat. Commun.*, 2024, **15**, 1711.

16 W. Luc, X. Fu, J. Shi, J. Lv, M. Jouny, B. H. Ko, Y. Xu, Q. Tu, X. Hu, J. Wu, Q. Yue, Y. Liu, F. Jiao and Y. Kang, *Nat. Catal.*, 2019, **2**, 423–430.

17 Y. Ji, Z. Chen, R. Wei, C. Yang, Y. Wang, J. Xu, H. Zhang, A. Guan, J. Chen, T. Sham, J. Luo, Y. Yang, X. Xu and G. Zheng, *Nat. Catal.*, 2022, **5**, 251–258.

18 R. Dorakhan, I. Grigioni, B. H. Lee, P. Ou, J. Abed, C. O'Brien, A. Rasouli, M. Plodinec, R. K. Miao, E. Shirzadi, J. Wicks, S. Park, G. Lee, J. Zhang, D. Sinton and E. H. Sargent, *Nat. Sustain.*, 2023, **2**, 448–457.

19 J. Ding, F. Li, X. Ren, Y. Liu, Y. Li, Z. Shen, T. Wang, W. Wang, Y. Wang, Y. Cui, H. Yang, T. Zhang and B. Liu, *Nat. Commun.*, 2024, **15**, 3641.

20 X. Ma, T. Yang, D. He, X. Gao, W. Jiang, D. Li, Y. Sun, X. Lin, J. Xu, H. Wang, X. Tai, Y. Lin, T. Yao, H. Zhou and Y. Wu, *Nat. Sustain.*, 2024, **4**, 53–66.

21 X. Yang, B. Ouyang, L. Zhao, Q. Shen, G. Chen, Y. Sun, C. Li and K. Xu, *J. Am. Chem. Soc.*, 2023, **145**, 27010–27021.

22 S. Ruan, B. Zhang, J. Zou, W. Zhong, X. He, J. Lu, Q. Zhang, Y. Wang and S. Xie, *Chin. J. Catal.*, 2022, **43**, 3161–3169.

23 L. Bian, Z. Zhang, H. Tian, N. Tian, Z. Ma and Z. Wang, *Chin. J. Catal.*, 2023, **54**, 199–211.

24 H. Li, P. Wei, T. Liu, M. Li, C. Wang, R. Li, J. Ye, Z. Zhou, S. Sun, Q. Fu, D. Gao, G. Wang and X. Bao, *Nat. Commun.*, 2024, **15**, 4603.

25 Y. Yang, S. Louisia, S. Yu, J. Jin, I. Roh, C. Chen, M. V. Fonseca Guzman, J. Feijóo, P. Chen, H. Wang, C. J. Pollock, X. Huang, Y. Shao, C. Wang, D. A. Muller, H. D. Abruña and P. Yang, *Nature*, 2023, **614**, 262–269.

26 X. Xu, Y. Zhong, M. Wajrak, T. Bhatelia, S. P. Jiang and Z. Shao, *InfoMat*, 2024, **6**, e12608.

27 Y. Zhang, K. Qi, P. Lyu, E. Petit, H. Wu, W. Wang, J. Ma, Y. Wang, C. Salameh and D. Voiry, *ACS Nano*, 2024, **18**, 17483–17491.

28 J. Ding, Q. Song, L. Xia, L. Ruan, M. Zhang, C. Ban, J. Meng, J. Ma, Y. Feng, Y. Wang, X. Tao, D. Yu, J. Dai, L. Gan and X. Zhou, *Nano Energy*, 2024, **128**, 109945.

29 W. Niu, Z. Chen, W. Guo, W. Mao, Y. Liu, Y. Guo, J. Chen, R. Huang, L. Kang, Y. Ma, Q. Yan, J. Ye, C. Cui, L. Zhang, P. Wang, X. Xu and B. Zhang, *Nat. Commun.*, 2023, **14**, 4882.

30 B. Zhang and J. Jiang, *Energy Environ. Mater.*, 2024, **7**, e12738.

31 S. Nitopi, E. Bertheussen, S. B. Scott, X. Liu, A. K. Engstfeld, S. Horch, B. Seger, I. E. L. Stephens, K. Chan, C. Hahn, J. K. Nørskov, T. F. Jaramillo and I. Chorkendorff, *Chem. Rev.*, 2019, **119**, 7610–7672.

32 P. D. Luna, R. Q. Bermudez, C. T. Dinh, M. B. Ross, O. S. Bushuyev, P. Todorović, T. Regier, S. O. Kelley, P. Yang and E. H. Sargent, *Nat. Catal.*, 2018, **8**, 103–110.

33 G. Kresse and J. Hafner, *Phys. Rev. B: Condens. Matter Mater. Phys.*, 1993, **49**, 14251.

34 G. Kresse and J. Hafner, *Phys. Rev. B: Condens. Matter Mater. Phys.*, 1993, **47**, 558.

35 G. Kresse and J. Furthmüller, *Phys. Rev. B: Condens. Matter Mater. Phys.*, 1996, **54**, 11169.

36 G. Kresse and D. Joubert, *Phys. Rev. B: Condens. Matter Mater. Phys.*, 1999, **59**, 1758.

37 S. Grimme, *J. Comput. Chem.*, 2006, **27**, 1769–1897.

38 R. Baghi, G. R. Peterson and L. J. Hope-Weeks, *J. Mater. Chem. A*, 2013, **1**, 10898–10902.

39 P. De Luna, R. Quintero-Bermudez, C. Dinh, M. B. Ross, O. S. Bushuyev, P. Todorović, T. Regier, S. O. Kelley, P. Yang and E. H. Sargent, *Nat. Catal.*, 2018, **1**, 103–110.

40 H. An, L. Wu, L. D. B. Mandemaker, S. Yang, J. de Ruiter, J. H. J. Wijten, J. C. L. Janssens, T. Hartman, W. van der Stam and B. M. Weckhuysen, *Angew. Chem., Int. Ed.*, 2021, **60**, 16576–16584.

41 X. Wang, Y. Chen, F. Li, R. K. Miao, J. E. Huang, Z. Zhao, X. Li, R. Dorakhan, S. Chu, J. Wu, S. Zheng, W. Ni, D. Kim, S. Park, Y. Liang, A. Ozden, P. Ou, Y. Hou, D. Sinton and E. H. Sargent, *Nat. Commun.*, 2024, **15**, 616.

42 J. Li, Y. Kuang, X. Zhang, W. Hung, C. Chiang, G. Zhu, G. Chen, F. Wang, P. Liang and H. Dai, *Nat. Catal.*, 2023, **6**, 1151–1163.

43 M. Zheng, P. Wang, X. Zhi, K. Yang, Y. Jiao, J. Duan, Y. Zheng and S. Qiao, *J. Am. Chem. Soc.*, 2022, **144**, 14936–14944.

44 Y. Rong, T. Liu, J. Sang, R. Li, P. Wei, H. Li, A. Dong, L. Che, Q. Fu, D. Gao and G. Wang, *Angew. Chem., Int. Ed.*, 2023, **62**, e202309893.

45 Y. Rong, X. Guo, G. Zhang, J. Sang, H. Li, D. Gao and G. Wang, *ACS Energy Lett.*, 2024, **9**, 3204–3211.

46 W. Zhi, X. Zhang, P. Yang, Z. Niu, F. Gao, Y. Zhang, L. Chi, S. Sun, J. DuanMu, P. Lu, Y. Li and M. Gao, *J. Am. Chem. Soc.*, 2023, **145**, 24338–24348.

47 J. Jin, J. Wicks, Q. Min, J. Li, Y. Hu, J. Ma, Y. Wang, Z. Jiang, Y. Xu, R. Lu, G. Si, P. Papangelakis, M. Shakouri, Q. Xiao, P. Ou, X. Wang, Z. Chen, W. Zhang, K. Yu, J. Song, X. Jiang, P. Qiu, Y. Lou, D. Sinton, L. Mai, E. H. Sargent and Y. Pang, *Nature*, 2023, **617**, 724–729.